INORGANIC CHEMISTRY FRONTIERS

RESEARCH ARTICLE

View Article Online
View Journal | View Issue

Cite this: *Inorg. Chem. Front.*, 2023, **10**, 2742

Electrophilicity modulated targeted luminescence of MOF-coated cotton composite for dual analyte detection in aqueous medium†

Abhijeet Rana and Shyam Biswas *

Sulfur is a soft Lewis base and thiocarbonyl has moderate electrophilicity. Our probe's properties are adjusted in such a way that it could simultaneously detect a Lewis acid (Hg^{2+}) and a strong nucleophile (NH_2–NH_2). Considering the above fact, a thioureido-functionalized robust MOF material was prepared, which was utilized for the selective fluorometric detection of environmentally significant toxic pollutants (Hg^{2+} and NH_2–NH_2) in an aqueous medium. The probe detected mercury by quenching the fluorescence emission intensity in a static pathway by soft-soft interaction with the S-atom of the probe. In contrast, the detection of hydrazine was furnished by a reaction-based pathway by the attack of hydrazine to the moderate electrophilic (thiocarbonyl) part of the probe, which resulted in an enhancement in the fluorescence emission intensity of the probe. A MOF-coated cotton composite was developed for the naked-eye detection of Hg^{2+} and NH_2–NH_2 for real-life applicability. The MOF was highly sensitive towards detecting Hg^{2+} and NH_2–NH_2 with very low detection times, *i.e.*, 10 s and 50 s, respectively. The probe's sensitivity also remained unaltered under a significantly lower concentration of the targeted analytes, *i.e.*, the detection limits for NH_2–NH_2 and Hg^{2+} were 1.9 nM and 4.0 nM, respectively. Our probe's response time and LOD are much lower than the other previously reported probes for Hg^{2+} and NH_2–NH_2 to date. A 92% fluorescence quenching and 28-fold fluorescence enhancement of the MOF were observed after the interaction of the probe with Hg^{2+} and NH_2–NH_2, respectively. The probe has excellent selectivity over the competitive analytes of Hg^{2+} and NH_2–NH_2. The MOF could also sense hydrazine in various environmental water specimens. Systematic mechanistic investigations were conducted to know the phenomena behind the fluorescence quenching and enhancement processes.

Received 1st February 2023,
Accepted 27th March 2023

DOI: 10.1039/d3qi00206c

rsc.li/frontiers-inorganic

Introduction

Mercury is a toxic soft Lewis acid present in many forms in the environment.[1] Once inorganic mercury comes into the environment, it is converted to methylmercury,[2] which enters the human body *via* sea food consumption[3] and causes Minamata disease. Hyperconcentration of mercury affects the heart, kidney, nervous system, and liver.[4,5] Therefore, USA EPA has set the highest concentration limit of mercury in water as 2 ppb. Hence, the selective detection of mercury below the limits set by USA EPA is highly required.

Hydrazine is used as a catalyst,[6] propellant,[7,8] blowing agent,[9] *etc*. The accumulation of hydrazine into the environment occurs though the discharge of industrial waste. Overexposure to hydrazine can cause detrimental effects on human health. The threshold concentration of hydrazine in drinking water has been set as 10 ppb.[10] Therefore, the detection of hydrazine below the safe limit is highly required.

Looking into the detrimental effects of mercury and hydrazine in drinking water, many environmental scientists working in the field of sensing hazardous materials have put forward their contribution by several methods. The selective sensing of hazardous materials has been reported by enormous research groups with the help of ion-exchange chromatography, electrochemical,[11] spectrometry,[12] voltammetry,[13] and fluorescence-based methods[38].[14–16] Among the abovementioned techniques, the fluorescence-based method has several advantages over other techniques due to the easy handling and simple observation process.[17] There are many class of materials utilized for the sensing of hazardous materials including quantum dots,[18,19] graphene oxide-based materials,[20] carbon nanotubes,[21] and organic probes.[22] Metal–organic frameworks (MOFs) are porous with very high surface areas and their active

Department of Chemistry, Indian Institute of Technology Guwahati, Guwahati, 781039 Assam, India. E-mail: sbiswas@iitg.ac.in

†Electronic supplementary information (ESI) available: E-SEM images, EDX, NMR, IR, TRPL, XPS and fluorescence spectra, N_2 sorption isotherm, XRPD patterns, digital images, TG curves, comparison tables. See DOI: https://doi.org/10.1039/d3qi00206c

sites for sensing could be easily tuned. Therefore, MOF-based materials are advantageous over other classes of materials.

The abovementioned toxic properties of hydrazine and mercury and the easy handling fluorescence method inspired us to develop a fluorescence-based selective probe to detect mercury and hydrazine. The soft nature of mercury pushed us to design a soft center-based probe with sulfur-containing functionality. In contrast, the nucleophilic nature of hydrazine having alpha-effect inspired us to design a probe with moderate electrophilic center. The moderate electrophilic nature guides the probe to selectively react with hydrazine even in the presence of other nucleophilic congeners. The above idea was incorporated by designing a thioureido-functionalized robust Hf-MOF named as **Hf-UiO-66-NHCSNHCH$_3$**. The soft sulfur atom and moderate electrophilic thiocarbonyl group was the active centers for the selective interaction of Hg^{2+} and NH_2–NH_2 with the probe. A 28-fold increment in the fluorescence intensity of **Hf-UiO-66-NHCSNHCH$_3$** was observed after the addition of hydrazine solution and a fluorescence quenching efficiency of 92% was observed after adding an aqueous Hg^{2+} solution . The probe can detect Hg^{2+} and NH_2–NH_2 below the permissible limit in drinking water. A thorough study of the mechanistic pathway was explored *via* various analytical techniques to present the work systematically and be applicable in future endeavours. The selectivity and applicability for real field purposes, the ultralow detection limit, and the relevance of dual sensing purpose make our material a unique sensor of mercury and hydrazine.

Experimental section

Chemicals and general methods

Related reagents and instruments have been mentioned in the ESI.†

Synthesis of $[Hf_6O_4(OH)_4(C_{10}H_8N_2O_4S)_{2.8}(C_8H_5NO_4)_{3.2}]\cdot 1H_2O$

The synthesis of the probe **Hf-UiO-66-NHCSNHCH$_3$** was initiated from a solvothermal synthesis of Hf(IV) metal salt and BDC-NH_2 linker-based MOF. The UiO-66 topology-based Hf(IV) MOF bearing BDC-NH_2 (BDC-NH_2: 2-amino-1,4-benzene dicarboxylic acid) ligand, *i.e.*, **Hf-UiO-66-NH$_2$** was synthesized by a systematic solvothermal approach. A mixture of $HfCl_4$ (0.54 mM) and BDC-NH_2 linker (0.75 mM) in 15 mL DMF using 1 mL HCl as a modulator was heated at 80 °C for 24 h. The precipitate was collected after 24 h and was appropriately washed with water and then with acetone. The obtained material was solvent exchanged with methanol for 24 h and then vacuum dried at 100 °C for 24 h to get the activated form of **Hf-UiO-66-NH$_2$**, *i.e.*, **Hf-UiO-66-NH$_2$**. In the second step, a post-synthetic modification approach was taken forward utilizing a mixture of 60 mg **Hf-UiO-66-NH$_2$** and 20 mg methyl isothiocyanate in a mixture of solvent ($CHCl_3$: CH_3OH = 9 : 1) and was heated at 55 °C for 3 days, as shown in Scheme 1.

Results and discussion

Characterization of $[Hf_6O_4(OH)_4(C_{10}H_8N_2O_4S)_{2.8}(C_8H_5NO_4)_{3.2}]\cdot 1H_2O$

During the post-synthetic modification of **Hf-UiO-66-NH$_2$** with methyl isothiocyanate, the –NH_2 group of **Hf-UiO-66-NH$_2$** was expected to react with the $H_3CN{=}C{=}S$ functionality to provide the –NH(C=S)$NHCH_3$ group. When the post-synthetically modified MOF named **Hf-UiO-66-NHCSNHCH$_3$** was digested with 40% HF solution, 46% conversion of the –NH_2 group to the –NH(C=S)$NHCH_3$ functionality could be noticed by comparing the digested ^{1}H NMR spectra of **Hf-UiO-66-NHCSNHCH$_3$** and **Hf-UiO-66-NH$_2$** (Fig. S1 and S2†). The ^{1}H NMR spectra of **Hf-UiO-66-NH$_2$** showed the presence of two doublets and one singlet due to three aromatic protons at 7.76 (d, 1H), 7.37 (S, 1H), and at 7.03 (D, 1H). The ^{1}H NMR spectra of **Hf-UiO-66-NHCSNHCH$_3$** showed three additional peaks at 8.05 (d, 1H), 7.95 (S, 1H), and 7.78 (D, 1H) including three aromatic protons of Hf-UiO-66-NH_2 and a singlet at 3.65 (S, 3H) due to three methyl protons. A downfield chemical shift was observed after post-synthetic modification as the binding of methyl isothiocyanate to the free amine group causes a decreased electron density in the benzene ring. The presence of six aromatic protons proved that some amount of the BDC-NH_2 linker is reacted with the methyl isothiocyanate group to afford 46% post-synthetic modification. Again, the presence of the peak due to the methyl group is direct evi-

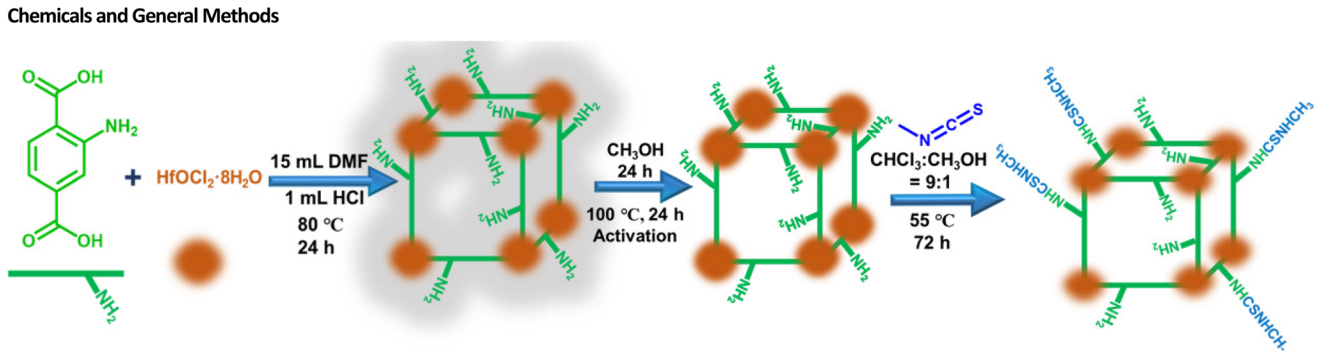

Scheme 1 Detailed stepwise synthesis of **Hf-UiO-66-NHCSNHCH$_3$**.

dence of the successful post-synthetic modification. The percentage of post-synthetic modification that occurred was calculated by comparing the area under each proton. Again, the ^{13}C NMR spectra of **Hf-UiO-66-NH$_2$** (^{13}C NMR: 169.3, 167.5, 150.5, 135.7, 132.0, 118.5, 116.1, 114.1) (Fig. S3†) and **Hf-UiO-66-NHCSNHCH$_3$** (^{13}C NMR: 175.9, 169.2, 167.3, 166.3, 163.3, 159.5, 151.0, 139.2, 136.8, 135.4, 131.7, 128.8, 124.45, 118.3, 116.9, 115.2, 113.1) (Fig. S4†) were compared. The additional peak at 175 ppm due to the thiocarbonyl group in the ^{13}C NMR spectrum of **Hf-UiO-66-NHCSNHCH$_3$** also supported the successful bonding between the amine of **Hf-UiO-66-NH$_2$** with the methyl isothiocyanate moiety.[23] The mass spectrometry of the digested MOF **Hf-UiO-66-NH$_2$** showed the presence of a strong peak at 180 *m*/*z*, which is due to the linker from the digested MOF (Fig. S5†), and the mass spectrum of **Hf-UiO-66-NHCSNHCH$_3$** displayed *m*/*z* peaks at 180 as well as 253 due the presence of both the linkers BDC-NH$_2$ and BDC-NHCSNHCH$_3$ (Fig. S6†). The above result is a strong evidence of the successful post-synthetic modification.

The FT-IR spectra of **Hf-UiO-66-NH$_2$** MOF possesses two peaks (at 1575 and 1385 cm^{-1}) due to the asymmetric and symmetric stretching frequency of the carboxylic group of **Hf-UiO-66-NH$_2$**. These two carboxyl frequencies are present in **Hf-UiO-66-NHCSNHCH$_3$** MOF, which proves that there is no structural detachment of the carboxylate from the metal center during post-synthetic modification. The FT-IR spectra showed additional peaks at 1280, 1085, and 798 cm^{-1} due to the –C═S bond of **Hf-UiO-66-NHCSNHCH$_3$** MOF,[24] which confirmed the successful post-synthetic modification (Fig. S7†).

The FE-SEM images (Fig. 1d) of **Hf-UiO-66-NHCSNHCH$_3$** and **Hf-UiO-66-NH$_2$** demonstrate similar particles, which confirmed no change in the crystallinity of the material after post-synthetic modification. The successful post-synthetic modification was again supported by the EDX elemental analysis. The TEM-EDX elemental analysis of **Hf-UiO-66-NH$_2$** confirmed the presence of Hf (5.1%) (Fig. S8†). At the same time, the TEM-EDX elemental analysis of **Hf-UiO-66-NHCSNHCH$_3$** confirmed the presence of Hf (4.6%) and S (4.5%) elements (Fig. S10†). The TEM-EDX elemental mapping was also carried out for **Hf-UiO-66-NH$_2$** and **Hf-UiO-66-NHCSNHCH$_3$**, which displayed the homogenous distribution of all the desired elements (Fig. S9 and S11†). The presence of the additional sulfur atom in **Hf-UiO-66-NHCSNHCH$_3$** confirmed the incorporation of the isothiocyanate group into the free amine of **Hf-UiO-66-NH$_2$**. The homogenous distribution of the desired elements in the elemental mapping of **Hf-UiO-66-NHCSNHCH$_3$** suggests that the methyl isothiocyanate molecule was not physically adsorbed on the surface of **Hf-UiO-66-NH$_2$** but it was bonded with the –NH$_2$ group of **Hf-UiO-66-NH$_2$**.

Further, the PXRD analysis of **Hf-UiO-66-NHCSNHCH$_3$** and **1′@NH$_2$** was performed to confirm their phase purity and crystallinity. Both materials showed similar PXRD patterns such as the simulated one (Fig. 1). The PXRD experiment demonstrated that the above-synthesized materials **Hf-UiO-66-NHCSNHCH$_3$** and **Hf-UiO-66-NH$_2$** belong to the UiO-66 topology. The Pawley fit and indexing data (Fig. S12 and Table S1†) of the slow scan PXRD data of **Hf-UiO-66-NHCSNHCH$_3$** again

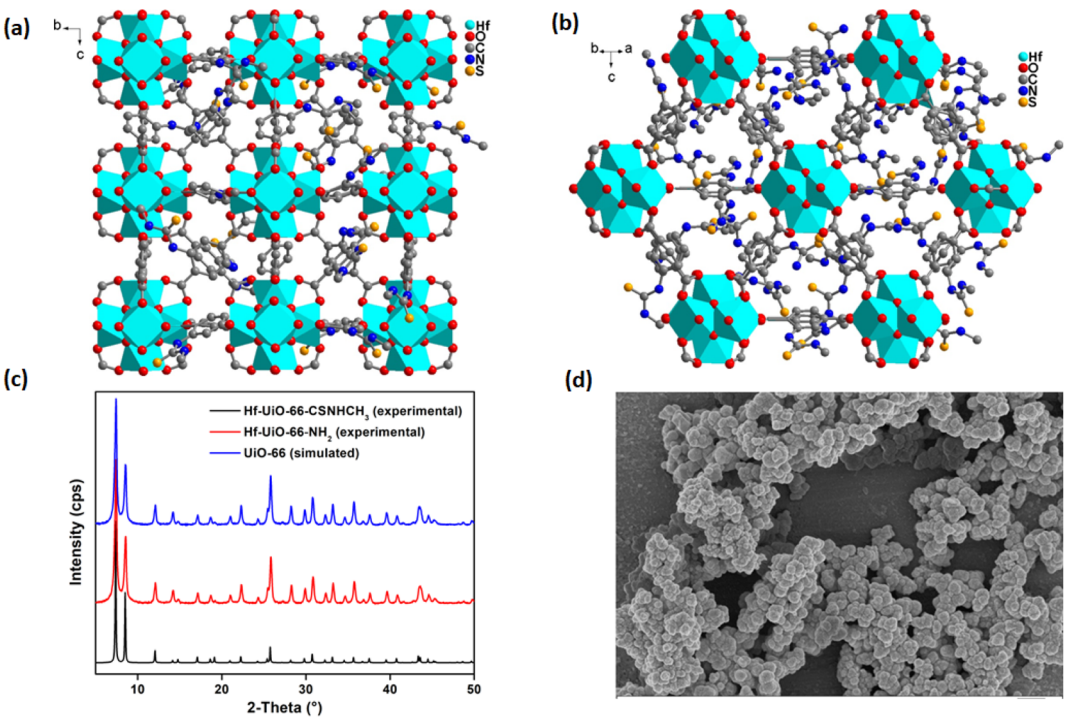

Fig. 1 (a) and (b) Simulated structure of **Hf-UiO-66-NHCSNHCH$_3$** with Hf atoms shown as cyan polyhedra. (c) Comparative PXRD pattern of **Hf-UiO-66-NHCSNHCH$_3$** with **Hf-UiO-66-NH$_2$** and UiO-66 MOF (simulated), (d) FE-SEM image of **Hf-UiO-66-NHCSNHCH$_3$**.

supported this observation. The Pawley fit data showed that the PXRD pattern of **Hf-UiO-66-NHCSNHCH$_3$** exactly fits with the simulated pattern with negligible errors (R_w = 1.0% and R_{wp} = 1.6%) (Fig. S12†).

The chemical robustness of the material was also examined by stirring the materials in DCM, DMF, H_2O, pH 2, and pH 12 solutions. The materials were filtered and the PXRD patterns of the recovered materials were measured individually. The PXRD pattern of the recovered materials precisely matched with the PXRD pattern of **Hf-UiO-66-NHCSNHCH$_3$** (Fig. S13†). It concludes that the crystallinity of the material remained unchanged even after 24 h of stirring.[37] Therefore, the probe **Hf-UiO-66-NHCSNHCH$_3$** is stable enough for the application of the sensing purpose in a variety of solvent media.

The thermogravimetric (TG) experiments for both **Hf-UiO-66-NHCSNHCH$_3$** and **Hf-UiO-66-NH$_2$** were performed to know the material's thermal stability. Initially, there was a weight loss of 2.9% in the TG-curve of **Hf-UiO-66-NH$_2$** due to the removal of 1.3 molecules of water per unit formula of **Hf-UiO-66-NH$_2$** at 130 °C (Fig. S14†). The second weight loss was attributed to the loss of the framework structure at 400 °C. The absence of breakpoint due to DMF in the TG trace confirmed the proper activation of **Hf-UiO-66-NH$_2$**. The material **Hf-UiO-66-NHCSNHCH$_3$** also displayed a similar TG-curve with an initial weight loss of 3.7% due to the loss 1.5 molecules of water per unit formula and the second weight loss due to linker dislocation from the framework structure starting from 350 °C to 400 °C. The framework destruction of **Hf-UiO-66-NHCSNHCH$_3$** occurred at a slightly lower temperature compared to **Hf-UiO-66-NH$_2$** due to the linker defect that arose at the time of post-synthetic modification.

N_2 sorption analysis of **Hf-UiO-66-NHCSNHCH$_3$** was carried out at −196 °C using liquid nitrogen. The determined surface area for **Hf-UiO-66-NHCSNHCH$_3$** was 498 $m^2\ g^{-1}$. We noticed a decreased surface area of **Hf-UiO-66-NHCSNHCH$_3$** compared to the surface area (784 $m^2\ g^{-1}$) of the previously reported **Hf-UiO-66-NH$_2$** MOF (Fig. S15†).[25] The reduced surface area is attributed to the post-synthetic modification. Because of post-synthetic transformation, the extra functionality of methyl isothiocyanate occupied the pores of **Hf-UiO-66-NH$_2$**, which caused a decrease in the surface area of **Hf-UiO-66-NHCSNHCH$_3$**. The decreased surface area of **Hf-UiO-66-NHCSNHCH$_3$** again supports the successful incorporation of the methyl isothiocyanate moiety *via* the free amine of **Hf-UiO-66-NH$_2$** (Fig. S16†).

Structural description

The PXRD pattern of the synthesized **Hf-UiO-66-NHCSNHCH$_3$** material agrees that the material belongs to the UiO-66 class (Fig. 1c). Again, the material's phase purity, crystallinity, and topology were supported by Pawley fit (Fig. S12†) and indexing (Table S1†). Due to the strong binding between the oxophilic hard Zr(IV) centers with the oxygen of the carboxylate groups of the linkers, the MOFs bearing Zr(IV) ions are usually robust. The hard–hard interaction gives rise to a chemically robust material. Initially, a secondary building unit (SBU) is formed by the bonding of six Zr(IV) ions to four of the oxygen and four hydroxy groups in the μ_3-bridging mode to afford one cuboctahedron oxo cluster.[26] Twelve of the BDC linkers bound to the SBU to give face-centered cubic topology with an approximate cell length of 20.7 Å.[27] The cell parameter of **Hf-UiO-66-NHCSNHCH$_3$** was found to be 20.74 Å by the indexing of its slow scan PXRD data (Table S1†). The overall face-centered cubic framework (Fig. 1a and b) possesses small tetrahedral cages and large octahedral cages.

Fluorescence sensing of Hg^{2+} and NH_2–NH_2

The use of mercury and hydrazine in industrial processes and their release into the environment creates numerous health-related issues. Therefore, the selective detection of industrially important toxic analytes is highly required for a healthy environment. Consequently, we synthesized a 2-(3-methylthioureido)terephthalic acid-functionalized targeted system for the selective detection of mercury and hydrazine. All the fluorescence experiments for the sensing of mercury were performed using a MOF suspension in DMF (1 mg mL^{-1}) and the analytes were prepared in water. The MOF suspension was prepared by taking 1 mg MOF in 1 mL DMF . The mixture was sonicated for about 30 min and kept undisturbed for 12 h. Afterward, the mixture was centrifuged and only the supernatant suspension was collected by decanting from the centrifuge tube and separating the excess MOF powder adhered below. In this way, we prepared the stable MOF suspension. A systematic fluorescence experiment was performed using 2700 μL DMF and 300 μL of the above-prepared MOF suspension and then adding 300 μL 10 mM aqueous analyte solution. For the detection of hydrazine, a similar procedure as that for mercury was followed with slight modification. Both MOF suspension and analyte solution were prepared in water, and all the fluorescence spectra were recorded using 2700 μL water and 300 μL MOF suspension and thereafter adding 300 μL 10 mM aqueous analyte solution. For all the fluorescence experiments for the detection of both mercury and hydrazine, fluorescent light of 360 nm wavelength was used for excitation, and the emission spectra were recorded between 380 and 600 nm. The excitation and emission spectra of the MOF suspension are displayed in Fig. S17.†

A volume-dependent fluorescence detection experiment was carried out by adding 50 μL 10 mM aqueous Hg^{2+} solution to 3000 μL MOF suspension in DMF in each step. A sudden quenching in the fluorescence emission intensity was observed after every incremental step and, finally, a saturation of the quenching process was noticed after the addition of 300 μL aqueous Hg^{2+} solution, as shown in Fig. 2a. A similar volume-dependent sensing experiment was carried out by adding 50 μL 10 mM aqueous hydrazine solution to 3000 μL aqueous MOF suspension in each step. An immediate turn-on in the fluorescence emission intensity was noticed after each incremental addition and, finally, a saturation in fluorescence intensity was detected after the addition of 300 μL 10 mM aqueous hydrazine solution, as displayed in Fig. 2b. The detection of targeted analytes should be reproducible and repeata-

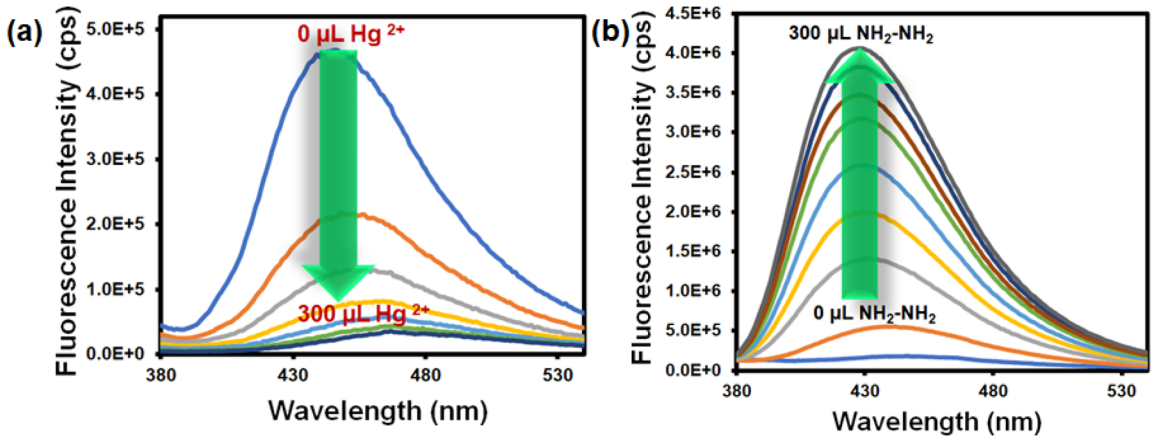

Fig. 2 Change in the fluorescence emission intensity of the probe **Hf-UiO-66-NHCSNHCH$_3$** after the incremental addition of 300 μL aqueous 10 mM Hg^{2+} (a) and NH_2–NH_2 (b) solution.

ble, which is a good characteristic of the ideal sensor material. Therefore, we carried out batch experiments multiple times on the same day and different days. The experimental results presented in Tables S2 and S3† confirmed that the sensing processes are reproducible and repeatable for providing the same results toward both the analytes with high precision and accuracy.

The time-dependent experiment was performed to determine the sensitivity of detection. To find the detection time, 300 μL 10 mM aqueous Hg^{2+} solution was added to a 3000 μL MOF suspension in DMF, and the fluorescence emission intensity was recorded after every 10 s intervals. We found that after 10 s, there was a saturation in the fluorescence intensity and no further appreciable quenching occurred up to 1 min (Fig. 3a and b). A similar procedure was adopted to find the probe's response time for hydrazine detection. In this case, we found that the turn-on nature of the fluorescence intensity of **Hf-UiO-66-NHCSNHCH$_3$** became saturated after 50 s (Fig. 3c

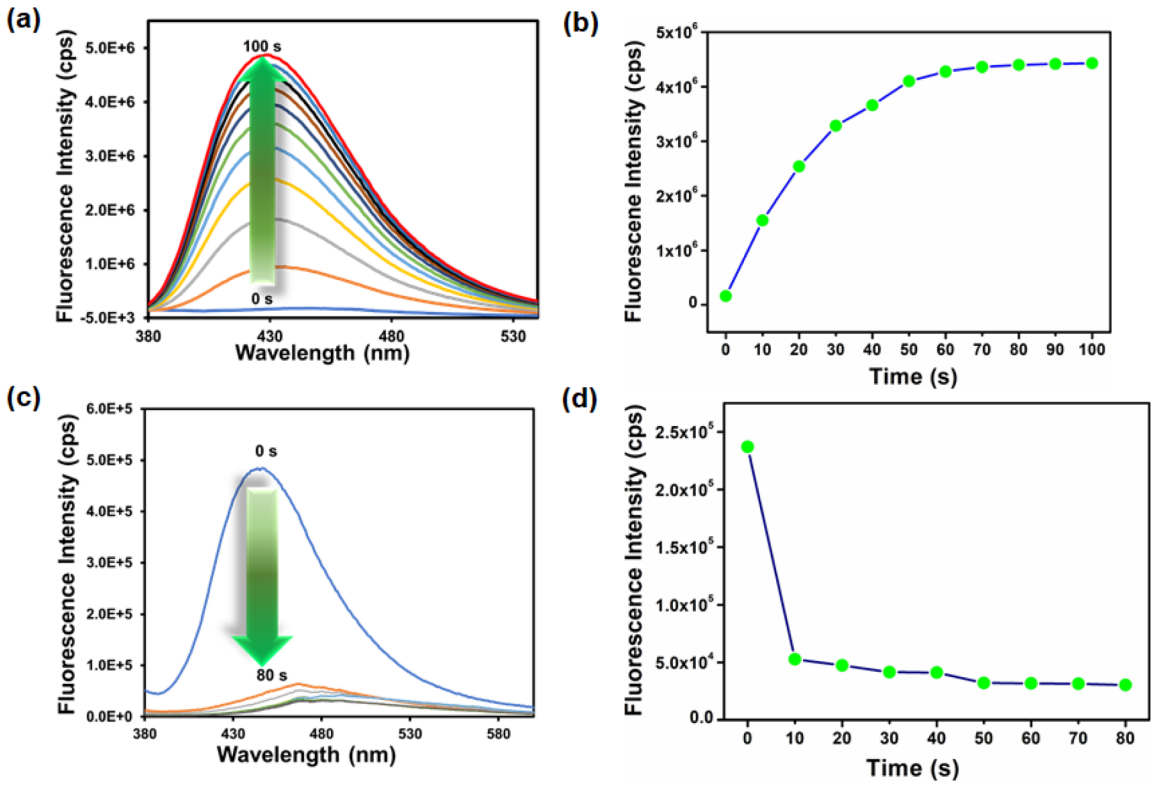

Fig. 3 Time-dependent fluorescence emission intensity of probe **Hf-UiO-66-NHCSNHCH$_3$** after the addition of 300 μL 10 mM aqueous solution of NH_2–NH_2 (a) and Hg^{2+} (c). Fluorescence intensity *versus* time plot for NH_2–NH_2 (b) and Hg^{2+} (d).

and d). Therefore, the probe **Hf-UiO-66-NHCSNHCH$_3$** is highly sensitive with a very low detection time as compared to other MOF-based mercury and hydrazine sensors displayed in Tables S5 and S6.† The fluorescence increment and quenching efficiency after adding 300 μL hydrazine and Hg^{2+} solution was calculated using the formulas I/I_0 and $(I - I_0/I) \times 100$, respectively (I_0 is the fluorescence intensity of the probe before the addition of the target analyte and I is the fluorescence intensity of the probe after the addition of the target analyte). We found a 28-fold increment in the fluorescence intensity of the probe after the addition of 300 μL 10 mM hydrazine solution. After the addition of 300 μL 10 mM Hg^{2+} solution, the fluorescence intensity of the probe quenched up to 92%. The appreciable change in the original fluorescence intensity of the probe by both the targeted analytes made our material a different and more efficient sensor.

The selectivity of the probe over the other competitive analytes was thoroughly investigated. To a MOF suspension of 3000 μL in DMF, 300 μL 10 mM of aqueous competitive analyte solutions (Ag^+, K^+, Li^+, Cd^{2+}, Zn^{2+}, Cu^{2+}, Mg^{2+}, Mn^{2+}, Pb^{2+}, Ni^{2+}, Na^+, Pt^{2+}, Pd^{2+}, Al^{3+}, Cr^{3+}, and Co^{3+}) were added in individual experiments, and the fluorescence intensity was recorded (Fig. 4a). We found a quenching efficiency of 92% in the case of Hg^{2+}, whereas for other analytes, the quenching efficiency only remained below 25% (Fig. S18–S33† and 4a). A similar experiment was performed using an aqueous MOF suspension and competitive analytes (ala, gly, leu, tyr, pro, urea, thiourea, phe, Br^-, F^-, CH_3COO^-, HSO_4^-, NCS^-, HCO_3^-, $S_2O_3^{2-}$, and NO_2^-) of hydrazine (Fig. S34–S49†). We found an immediate 28-fold increment in the fluorescence intensity when hydrazine was added to an aqueous MOF suspension. However, a minor enhancement in fluorescence intensity was noticed for other competitive analytes of hydrazine. The above experiments confirmed that the probe **Hf-UiO-66-NHCSNHCH$_3$** is highly selective over other competitive analytes for the selective detection of Hg^{2+} and hydrazine, as shown in Fig. 4b. An ideal probe should not only detect the target analyte selectively, but the detection process should also be repeatable and with a minimum allowed standard error. Therefore, the selectivity experiment was carried out three times, and the error in the 2D-bar plot is presented as the standard deviation in Fig. 4a and b. The minor standard deviations confirmed that our probe is reproducible in providing the results repeatedly with high precesion and accuracy.

We evaluated the selectivity of our probe to hydrazine and Hg^{2+} in a complex medium in the presence of other competitive analytes. A three-step procedure was carried out for the selectivity experiments. In the first step, the fluorescence emission intensity of the MOF suspension was recorded. In the second step, 300 μL 10 mM aqueous solution of a competitive analyte was added and the fluorescence spectrum was recorded. In the last step, 300 μL 10 mM aqueous Hg^{2+} solution was added and the fluorescence emission intensity was recorded. The same experiment was repeated for all the competitive analytes of Hg^{2+}. Similar experimental procedures were adopted for all the competitive analytes of hydrazine as well. The obtained results showed that probe **Hf-UiO-66-NHCSNHCH$_3$** can detect both Hg^{2+} and hydrazine selectively in the presence of respective competitors. As displayed in Fig. 5a and b, there is no such competitor analyte to question the selectivity of the probe **Hf-UiO-66-NHCSNHCH$_3$** for detecting both the targeted analytes (Hg^{2+} and NH_2–NH_2).

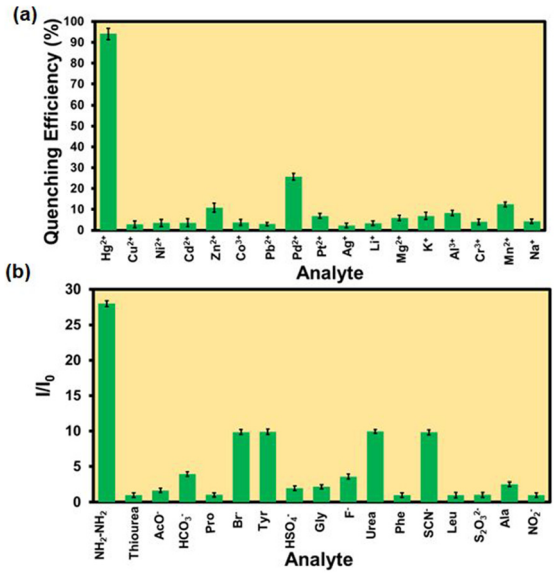

Fig. 4 Comparative selectivity bar plots of the probe **Hf-UiO-66-NHCSNHCH$_3$** toward Hg^{2+} (a) and NH_2–NH_2 (b) with their respective congeners (plots are shown with standard deviations of 3 measurements).

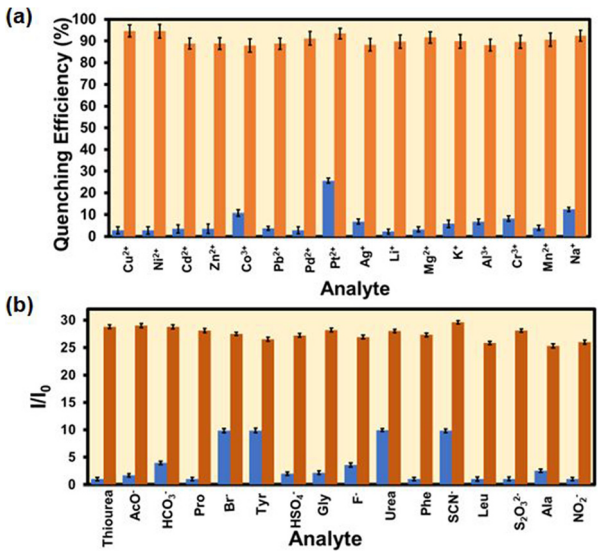

Fig. 5 The comparative selectivity bar plot (with standard deviations) of probe **Hf-UiO-66-NHCSNHCH$_3$** toward Hg^{2+} (a) and NH_2–NH_2 (b) in the presence of their respective congeners. The brown bars represent the quenching efficiency toward Hg^{2+} and fold increment in the case of NH_2–NH_2 and the blue bars belong to the competitive analytes.

The low value of limit of detection (LOD) is one of the essential properties of an ideal sensor. Therefore, we performed the fluorescence sensing experiment of **Hf-UiO-66-NHCSNHCH$_3$** of our probe toward detecting mercury and hydrazine in the concentration of analytes with as low concentration as possible. After a systematic investigation, we calculated the LOD values using the formula $3\sigma/k$. Here, σ is the standard deviation of the blank fluorescence intensities of the MOF suspension only and k is the slope of the curve (linear fit curve between fluorescence intensity and concentration) (Fig. S50 to S51†). The LOD values of the probe **Hf-UiO-66-NHCSNHCH$_3$** were 1.9 ± 0.25 nM and 4.0 ± 0.37 nM for hydrazine and Hg^{2+} detection, respectively. The obtained LOD values are lower in comparison with any MOF-based sensors of mercury and hydrazine to date (Tables S5 and S6†). The selectivity, sensitivity, and lower LOD value of our probe **Hf-UiO-66-NHCSNHCH$_3$** toward detecting mercury and hydrazine make it an ideal sensor.

To understand the quenching process of the probe by Hg^{2+}, we plotted the Stern–Volmer plot. The Stern–Volmer plot in Fig. S66† displays that at lower concentration, the plot is linear, but at higher concentration, it became steeper. The above observation concluded that the quenching process might be due to the static or dynamic pathway.[28] Therefore, we carried out the time-resolved fluorescence lifetime experiment. Again, the Stern–Volmer constant (K_{sv}) obtained from the slope of the plot between I_0/I *versus* the concentration of mercury confirmed that the quenching process must be due to strong interaction between the probe and mercury as the K_{sv} value is much higher (7.49×10^5 M^{-1}) (Table S1†). There was almost no change in the probe's lifetime before and after adding Hg^{2+}. The minor lifetime change confirmed that the static pathway of fluorescence quenching occurred due to the formation of the ground state complex between the probe and Hg^{2+} (Fig. S52 and Table S4†). The 3D-Stern–Volmer plot, also presented in Fig. 6, shows that the material is highly selective toward mercury over other analytes in a wide concentration range.

The recyclability of the probe for the sensing of mercury was examined by washing it with DMF and water after each cycle of the sensing process. We performed the recyclability experiment up to seven cycles, which showed that the probe is equally efficient in detecting mercury up to seven cycles, as shown in Fig. S53.†

The sensing of hydrazine in different water specimens was studied in a systematic way. An MOF suspension was prepared in each water specimen (river water, seawater, lake water, tap water, and distilled water). A series of aqueous hydrazine solutions of 3.33 mM, 6.66 mM, and 10 mM concentrations were prepared and utilized for sensing experiments. The fluorescence experiment was carried out in a general manner by recording the fluorescence emission intensity before and after the addition of different concentrations of hydrazine. The obtained results shown in Fig. 7a proved that our probe has efficiency in detecting hydrazine even from a complex water specimen system. These results indicate that the probe can work for real-field application purposes.

Again, the detection of hydrazine in different pH solutions was examined. The obtained results in Fig. 7b indicates that our probe could detect hydrazine in a wide pH range (pH 4 to pH 12). At pH 2, the presence of an acidic medium immediately protonated the added hydrazine and hindered its attack on the thiocarbonyl group. Therefore, a negligible turn-on in the fluorescence emission intensity was noticed after the addition of hydrazine to the MOF suspension.

A naked eye detection method was adopted by adding hydrazine and mercury to the cuvettes containing MOF suspension under a fluorescence lamp. A turn-on blue fluorescence light was observed after the addition of hydrazine, whereas after the addition of mercury, a turn-off in fluorescence was observed under the fluorescence lamp. A cotton composite-based device was also designed by coating MOF

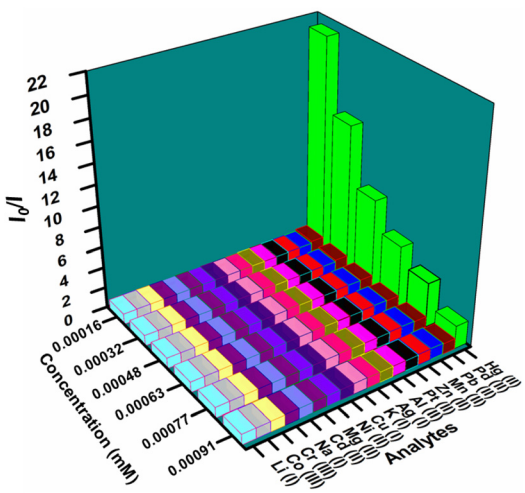

Fig. 6 3D Stern–Volmer plot for the detection of Hg^{2+}.

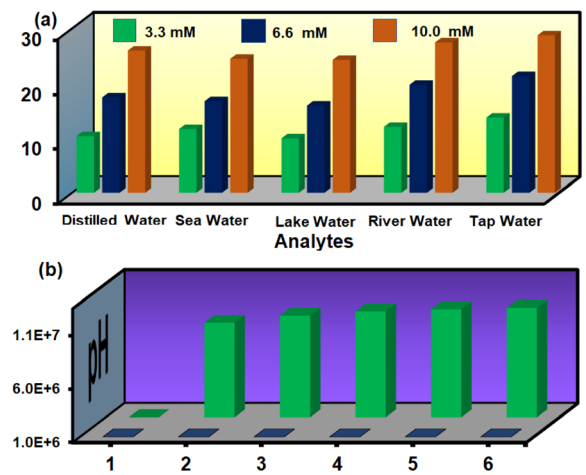

Fig. 7 Detection of hydrazine in environmental water specimens at different concentrations (a) and detection of hydrazine in various pH solutions (b).

powder onto the surface of a cotton cloth. For preparing the MOF-cotton composite, at first, cotton pieces were washed with ethanol and acetone and dried. The clean cotton pieces were immersed in MOF suspension in ethanol. The cotton pieces were stirred in MOF suspension slowly for 24 h. Then, the pieces were removed and dried in an oven. The dried MOF-cotton composite was utilized further for real-field sensing purposes. Cotton possesses free hydroxy groups on its surface, and the Hf-atom of **Hf-UiO-66-NHCSNHCH$_3$** is oxophilic in nature. Therefore, the MOF material was bound to the hydroxy groups on the surface of cotton to produce a useful cotton-composite material, which has great utilization for real-field sensing application purposes. After adding mercury and hydrazine to the MOF-coated cotton composite, similar turn-off and turn-on phenomena in fluorescence intensity were observed (Fig. 8). The simple cotton composite-based naked-eye sensing device made of our material applicable in real-world sensing applications.

Mechanism of hydrazine sensing

A systematic experimental investigation was performed to find the reason behind the selective turn-on detection of hydrazine by the **Hf-UiO-66-NHCSNHCH$_3$** probe. The PXRD analysis of the probe was performed after one cycle of sensing experiment and the retention of the exact PXRD pattern before and after sensing confirmed that the turn-on behaviour of the probe was not due to the structural destruction of the MOF material (Fig. S54†). The recyclability experiment was performed using the recovered material after the first cycle of the sensing experiment. The fluorescence spectrum of the recovered probe showed a turn-on nature before adding hydrazine solution. The above result confirmed that a new species was generated due to the reaction between the functional group of the probe and hydrazine. Therefore, the fluorescence turn-on occurred by a reaction-based pathway.

To know the exact active center of the reaction, we carried out sensing experiments with **Hf-UiO-66-NH$_2$** MOF. The obtained result showed that after adding hydrazine solution to **Hf-UiO-66-NH$_2$** suspension, there was little change in the fluorescence emission intensity. The above result indicated that the reaction between the thiocarbonyl group of the probe and hydrazine is the reason behind the fluorescence turn-on behavior. Again, we repeated the fluorescence sensing experiment utilizing a **Hf-BDC-NHCON(CH$_3$)$_2$** MOF in place of our probe **Hf-UiO-66-NHCSNHCH$_3$**. In this case, a similar fluorescence turn-on behavior such as probe **Hf-UiO-66-NHCSNHCH$_3$** was observed (Fig. 9). The probe **Hf-BDC-NHCON(CH$_3$)$_2$** is not selective for other competitive analytes such as NCS^-, HSO_4^-, and $S_2O_3^{2-}$. **Hf-BDC-NHCON(CH$_3$)$_2$** showed a similar turn-on behaviour similar to NH_2–NH_2. The higher electrophilicity of **Hf-BDC-NHCON(CH$_3$)$_2$** is the cause of the absence of selectivity, whereas with probe **Hf-UiO-66-NHCSNHCH$_3$**, the moderate electrophilicity of the thiocarbonyl group helps to detect hydrazine without any selectivity issue. The α-effect of hydrazine causes the nucleophilic attack on the thiocarbonyl group. It breaks the conjugation from the aromatic part of the linker, resulting in an enhancement in the fluorescence emission intensity. Further proof of reaction-based nucleophilic attack on the thiocarbonyl functionality of the linker was supported by the ^{1}H NMR and ^{13}C NMR spectra. The aromatic peaks in the ^{1}H NMR spectrum of hydrazine-treated **Hf-UiO-66-NHCSNHCH$_3$** displayed an up-field chemical shift due to an increase in the electron density on the benzene ring (Fig. S55†). In the ^{13}C NMR spectrum, the disappearance of the peak at 175 ppm and the appearance of the 149 ppm peak is a strong evidence of the nucleophilic attack by NH_2–NH_2 (Fig. S56†). The mass spectrum of the probe after the addition of hydrazine showed prominent peaks at 237 and 251 m/z ratios (Fig. S57†), which is due to the formation of the new imine complex (mass 251) by the attack of hydrazine on the thiocarbonyl group. Later, the imine complex dissociated by the attack of water present in the system to give a carbonyl compound (mass 237), as shown below in Scheme 2. Again, the UV-Vis spectra of probe **Hf-UiO-66-NHCSNHCH$_3$** before and after the addition of NH_2–NH_2 was examined. We noticed a considerable change in the absorbance spectrum after adding NH_2–NH_2. It also supports that the enhancement in the fluorescence emission intensity of the probe **Hf-UiO-66-NHCSNHCH$_3$** after adding NH_2–NH_2 might be due to a reaction-based pathway (Fig. S58†).

The EDX elemental analysis of the recovered probe after hydrazine sensing confirmed the absence of sulfur atoms, indicating a nucleophilic attack by hydrazine on the thiocarbonyl group of the probe, thereby causing loss of sulfur in the form of hydrogen sulfide (H_2S) (Fig. S59†). To confirm the removal of sulfur in the form of H_2S, we used a previously reported azide-based H_2S sensor **Nap-but** for H_2S detection.[29] The H_2S sensor was spiked with our MOF suspension, and the

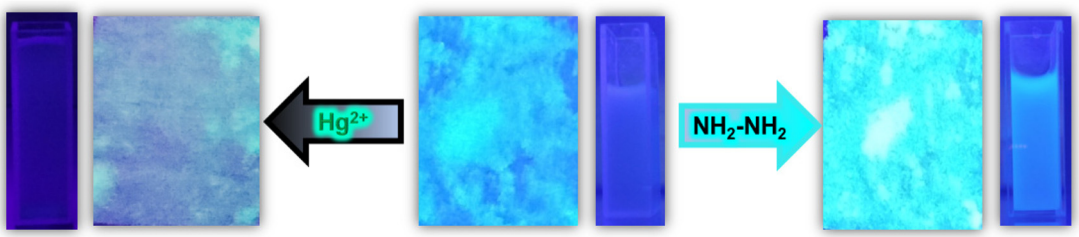

Fig. 8 Naked eye detection of Hg^{2+} and NH_2–NH_2 by MOF-coated cotton composite under a fluorescence lamp.

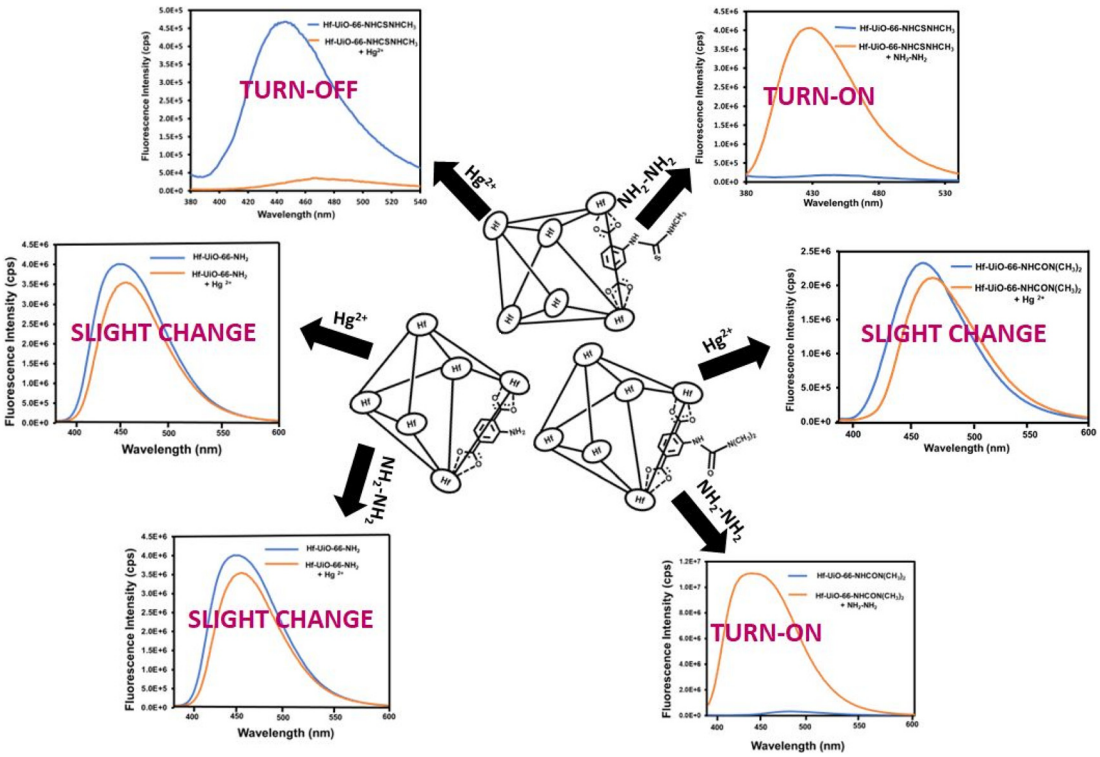

Fig. 9 Schematic representation of the change in the fluorescence emission intensity of **Hf-UiO-66-NHCSNHCH$_3$**, **Hf-UiO-66-NH$_2$**, and **Hf-UiO-66-NHCON(CH$_3$)$_2$** before and after the addition of Hg^{2+} and NH_2–NH_2.

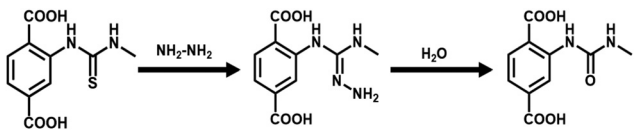

Scheme 2 Proposed mechanism of hydrazine sensing by the probe **Hf-UiO-66-NHCSNHCH$_3$**.

fluorescence spectrum was recorded. The same was also utilized by Bhabak *et al.* to detect the H_2S from their reaction medium.[30] After the addition of hydrazine to the above mixture, we noticed a prominent enhancement in the fluorescence intensity, which confirmed the release of H_2S from our probe due to the attack of hydrazine on the thiocarbonyl part of our probe (Fig. S60†). When we added hydrazine to a mixture of our probe and lead acetate in water, we noticed immediate black precipitation due to the formation of lead sulfide (Fig. S61†).[31] The source of sulfur must be due to the detachment of sulfur from our probe. As we know, lead acetate is very reactive toward H_2S to form lead sulfate. The color of lead sulfate is black, and we noticed a black sediment in the mixed suspension after adding hydrazine. All the above experimental data strongly supported the nucleophilic attack of hydrazine to the thiocarbonyl center of our probe. It caused an enhancement in the fluorescence emission intensity after adding hydrazine to the probe.

Mechanism of Hg^{2+} sensing

A significant quenching in the fluorescence spectrum of **Hf-UiO-66-NHCSNHCH$_3$** by mercury inspired us to explore the sensing mechanism of our probe toward mercury. The fluorescence quenching mechanism is very crucial from a chemist's perspective. Therefore, we conducted a series of experiments to find the exact reason behind the quenching process. As mentioned above, the probe is recyclable, and the PXRD pattern remained unchanged after sensing (Fig. S62†), proving that the fluorescence quenching process is neither due to a reaction-based process nor due to the structural destruction of the framework structure. Further, the EDX spectrum of the probe after sensing and thorough washing did not show Hg^{2+} or loss of any element, which also supported the above statement that the quenching process is neither due to a reaction-based process nor due to the structural destruction of the framework (Fig. S63†). The washing process was carried out by stirring the recovered sample in water for 24 h, followed by filtration and drying for further use. The recovered sample after the sensing of Hg^{2+} without washing showed the presence of Hg^{2+} in the EDS (TEM) spectrum and elemental mapping, which confirmed the weak complexation between the probe and Hg^{2+} (Fig. S64 and S65†). The Stern–Volmer plot mentioned above is linear at lower concentration and became steeper at higher concentration of mercury, which may be due to a static or dynamic quenching pathway. To summarize, we carried out the fluorescence lifetime study of probe **Hf-UiO-66-NHCSNHCH$_3$** before and after adding Hg^{2+}.

The fluorescence lifetime of the probe remained almost the same before and after adding mercury solution to the MOF suspension, as mentioned above. Therefore, the quenching process was not due to a dynamic pathway which kicked out the possibility of fluorescence resonance energy transfer mechanism. The above result confirmed that the fluorescence quenching process occurred through a static quenching pathway, *i.e.*, due to the ground state complexation between the probe and mercury, which allows the electron transfer from the probe to the vacant orbital of mercury. As reported by many previous works, the sulfur atom of the thiocarbonyl group is the center for the interaction with mercury, and in our case, the sulfur of the probe may be the center for soft–soft interaction with mercury.[32] Therefore, we performed X-ray photoelectron spectroscopy to find the exact active center of complexation. We executed the XPS analysis of **Hf-UiO-66-NHCSNHCH$_3$** before and after interaction with mercury. The binding energies of the 2S orbital of sulfur were 161.96 and 163.09 eV before the interaction with mercury. They became 162.46 and 163.58 eV after the interaction with mercury, providing a direct support for the interaction of mercury with sulfur. The mercury–sulfur interaction allows the transfer of electrons from the probe to mercury and thereby causes quenching in the fluorescence intensity of the probe (Fig. S66†). The shift in the binding energy of all the elements after interaction with Hg^{2+} also supported that there must be some interaction between the probe and Hg^{2+} (Fig. S67–S70†). The presence of the XPS characteristic peak of mercury is also direct proof of the interaction between the sulfur atom of the probe and Hg^{2+} (Fig. S71†).[33] The solid state UV-Vis spectrum of our material before and after the addition of Hg^{2+} showed a 24 nm red shift, which is a strong evidence of ground state complexation between our probe and Hg^{2+} (Fig. S72†).

Further confirmation of molecular interaction was obtained from a systematic temperature-dependant fluorescence experiment of our probe in the presence of different concentrations of mercury in varying temperature range (298–343 K). The K_{sv} value was obtained at different temperatures from the linear fit plot of I/I_0 *versus* the concentration of mercury (Fig. S73†). There was a decrease in the K_{sv} value with an increase in temperature, as shown in Table 1. The reduction in the K_{sv} value with increase in temperature rise supports the soft-soft interaction between mercury and the sulfur atom of our probe.

Table 1 Thermodynamic parameters obtained from Stern–Volmer, modified Stern–Volmer, and Van't Hoff equations obtained from temperature-dependent fluorescence titration experiments in the presence of Hg^{2+} ion

T (K)	$K_{sv} \times 10^5$ (L mol^{-1})	$K_a \times 10^5$ (L mol^{-1})	ΔG (kJ mol^{-1})	ΔH (kJ mol^{-1})	ΔS (J mol^{-1} K^{-1})
298	7.49	1.29	−28.89	−37.24	−28.02
313	6.23	0.49	−28.47		
328	5.99	0.26	−28.05		
343	5.51	0.19	−27.63		

The bimolecular binding constant (K_a) at different temperatures was obtained from the intercept of the plot of $\log[(I_0 - I)/I]$ *versus* $\log[Q]$ using the modified Stern–Volmer equation (Fig. S74†): $\log[(I_0 - I)/I] = \log K_a + n \log[Q]$. The decrease in the magnitude of the binding constant again supported the fact that the quenching process was due to the soft-soft interaction between mercury and the sulfur atom of our probe (Table 1). By increasing the temperature of the system, the randomness of the system increases and the interaction becomes weak, because of which the value of the binding constant decreased with the increase in the temperature.[34,35]

The thermodynamic parameters, *i.e.*, enthalpy change (ΔH) and entropy change (ΔS), were obtained from the slope and intercept of the $\log K_a$ *versus* $1/T$ plot, respectively (Fig. S75†). As we know, the difference in enthalpy and entropy could help in predicting the interaction process. The positive value of ΔH and ΔS suggests hydrophobic interaction, whereas the negative value of ΔH and positive value of ΔS suggests electrostatic interaction. In our case, both the thermodynamic parameters are negative, indicating molecular interaction.

$$\ln K_a = -\Delta H/RT + \Delta S/R$$

Further, we calculated the free energy change (ΔG) at different temperatures using the obtained value of ΔH and ΔS and the following thermodynamic formula. The obtained values of ΔG at various temperatures were negative, which confirmed that the interaction process was spontaneous and exothermic.[36] The decrease in the magnitude of ΔG with an increase in temperature also agrees with the K_a values obtained at various temperatures.

$$\Delta G = \Delta H\ T\Delta S$$

Further, we carried out control fluorescence experiments using **Hf-UiO-66-NH$_2$** and **Hf-UiO-66-NHCON(CH$_3$)$_2$** MOF materials in place of our probe. A negligible quenching in fluorescence emission intensity was observed after adding mercury solution to **Hf-UiO-66-NH$_2$** and **Hf-UiO-66-NHCON(CH$_3$)$_2$** MOF suspensions (Fig. 9). The experiments again confirmed that the interaction between the sulfur atom of the probe and mercury is the reason behind the fluorescence quenching process.

Conclusion

The detection capacity of Hg^{2+} and NH_2–NH_2 by our probe was presented systematically with a proper explanation of the mechanism behind the change in the fluorescence emission intensities. The lower detection limit, fast response, recyclability, and reproducibility with high precession made our probe reliable over the other reported probes for Hg^{2+} and NH_2–NH_2 sensing. The cotton-based MOF composite is advantageous over the paper-strip device due to its low-cost and recyclable nature. The probe detects Hg^{2+} and NH_2–NH_2 in the presence of a wide variety of competitive analysts. The high turn-on in the fluorescence emission intensity (28-fold increment) due to

hydrazine and the high quenching efficiency (92%) made our probe ideal due to the noticeable change in the signal. The probe can also detect hydrazine from environmental water samples and a wide range of pH solutions. The detection mechanisms of Hg^{2+} and NH_2–NH_2 were explained in a systematic manner using appropriate analytical characterization methods, which is an essential criterion for a good sensor material. The overall work presented here will help scientists working in the field of MOF-based sensors due to the reliable and reproducible nature of our probe.

Author contributions

AR performed all the experiments and prepared the manuscript taking scientific ideas and advices from SB.

Conflicts of interest

There are no conflicts to declare.

Acknowledgements

The financial support for this work was obtained from SERB through grant no. CRG/2021/000080 and EEQ/2021/000013. We are grateful toward central instrumental facility, IIT Guwahati for providing instrumental support. AR is thankful to PMRF for providing economic support.

References

1 F. A. Cotton, G. Wilkinson, C. Murillo and M. Bochmann, *Advanced Inorganic Chemistry*, *John Wiley and Sons, Inc*, *New York*, 1999, 6, 590–629.
2 M. Li, A. T. Schartup, A. P. Valberg, J. D. Ewald, D. P. Krabbenhoft, R. Yin, P. H. Balcom and E. M. Sunderland, Environmental origins of methylmercury accumulated in subarctic estuarine fish indicated by mercury stable isotopes, *Environ. Sci. Technol.*, 2016, **50**, 11559–11568.
3 C. T. Driscoll, R. P. Mason, H. M. Chan, D. J. Jacob and N. Pirrone, Mercury as a global pollutant: sources, pathways, and effects, *Environ. Sci. Technol.*, 2013, **47**, 4967–4983.
4 R. K. B. Barvin, P. Prakash, V. Ganesh and B. Jeyaprabha, Highly selective and sensitive sensing of toxic mercury ions utilizing carbon quantum dot-modified glassy carbon electrode, *Int. J. Environ. Res. Public Health*, 2013, **13**, 1015–1023.
5 S. Ghosh, F. Steinke, A. Rana and S. Biswas, A fluorescent zirconium organic framework displaying rapid and nanomolar level detection of Hg(ii) and nitroantibiotics, *Inorg. Chem. Front.*, 2022, **9**, 859–869.
6 L. P. Kuhn, Catalytic reduction with hydrazine, *J. Am. Chem. Soc.*, 1951, **73**, 1510–1512.
7 J. B. Levy, G. V. Elbe, R. Friedman, T. Wallin and S. J. Adams, The deflagration of hydrazine perchlorate, *Adv. Propellants Chem.*, 1966, **54**, 55–72.
8 A. R. Katritzky, Hydrazine and its derivatives: preparation, properties, applications, *J. Am. Chem. Soc.*, 2002, **124**, 6504.
9 J. Singh, K. R. B. Singh, M. Kumar, R. Verma, R. Verma, P. Malik, S. Srivastava, R. P. Singh and D. Kumar, Melt-quenched vanadium pentoxide-stabilized chitosan nanohybrids for efficient hydrazine detection, *Mater. Adv.*, 2021, **2**, 6665–6675.
10 M. Sun, L. Bai and D. Q. Liu, A generic approach for the determination of trace hydrazine in drug substances using in situ derivatization-headspace GC-MS, *J. Pharm. Biomed. Anal.*, 2009, **49**, 529–533.
11 E. Bakker and M. T. Diaz, Electrochemical sensors, *Anal. Chem.*, 2002, **74**, 2781–2800.
12 L. Eilert, A. Schallmey and F. Kaspar, UV-spectroscopic detection of (pyro-)phosphate with the PUB module, *Anal. Chem.*, 2022, **94**, 3432–3435.
13 M. Michalak, M. Kurel, J. Jedraszko, D. Toczydlowska, G. Wittstock, M. Opallo and W. Nogala, Voltammetric pH nanosensor, *Anal. Chem.*, 2015, **87**, 11641–11645.
14 Y. Wu, X. Liu, Q. Wu, J. Yi and G. Zhang, Carbon nanodots-based fluorescent turn-on sensor array for biothiols, *Anal. Chem.*, 2017, **89**, 7084–7089.
15 A. Rana, S. Nandi and S. Biswas, Sulfonic acid functionalized zirconium-based metal–organic framework for the selective detection of copper(II) ions, *New J. Chem.*, 2022, **46**, 10477–10483.
16 A. Rana, C. Gogoi, S. Ghosh, S. Nandi, S. Kumar, U. Manna and S. Biswas, Rapid recognition of fatal cyanide in water in a wide pH range by a trifluoroacetamido based metal–organic framework, *New J. Chem.*, 2021, **45**, 20193–20200.
17 S. Ghosh, F. Steinke, A. Rana, M. Alam and S. Biswas, A metal-organic framework with allyloxy functionalization for aqueous-phase fluorescence recognition of Pd(II) ion, *Eur. J. Inorg. Chem.*, 2021, **2021**, 3846–3851.
18 Q. Fan, J. Li, Y. Zhu, Z. Yang, T. Shen, Y. Guo, L. Wang, T. Mei, J. Wang and X. Wang, Functional carbon quantum dots for highly sensitive graphene transistors for Cu2+ ion detection, *ACS Appl. Mater. Interfaces*, 2020, **12**, 4797–4803.
19 G. Mao, G. Wu, M. Chen, C. Y. C. Yan and X. Zhang, Synthesis of dual-emitting CdZnSe/Mn:ZnS quantum dots for sensing the pH change in live cells, *Anal. Chem.*, 2022, **94**, 6665–6671.
20 M. Li, T. Chen, J. J. Gooding and J. Liu, Review of carbon and graphene quantum dots for sensing, *ACS Sens.*, 2019, **4**, 1732–1748.
21 V. Schroeder, S. Savagatrup, S. L. M. He and T. M. Swager, Carbon nanotube chemical sensors, *Chem. Rev.*, 2019, **119**, 599–663.
22 A. K. Singh, A. V. Nair and N. D. P. Singh, Small two-photon organic fluorogenic probes: sensing and bioimaging of cancer relevant biomarkers, *Anal. Chem.*, 2022, **94**, 177–192.
23 A. Recchimurzo, C. Micheletti, G. Uccello-Barretta and F. Balzano, A dimeric thiourea CSA for the enantiodiscrimi-

nation of amino acid derivatives by NMR spectroscopy, *J. Org. Chem.*, 2021, **86**, 7381–7389.

24 C. Rao and R. Venkataraghavan, The C=S stretching frequency and the "−N−C=S bands" in the infrared, *Spectrochim. Acta, Part A*, 1989, **45**, 299–305.

25 Z. Hu, A. Nalaparaju, Y. Peng, J. Jiang and D. Zhao, Modulated hydrothermal synthesis of UiO-66 (Hf)-type metal–organic frameworks for optimal carbon dioxide separation, *Inorg. Chem.*, 2016, **55**, 1134–1141.

26 J. Winarta, B. Shan, S. M. Mcintyre, L. Ye, C. Wang, J. Liu and B. Mu, A decade of UiO-66 research: a historic review of dynamic structure, synthesis mechanisms, and characterization techniques of an archetypal metal–organic framework, *Cryst. Growth Des.*, 2019, **20**, 1347–1362.

27 L. Valenzano, B. Civalleri, S. Chavan, S. Bordiga, M. H. Nilsen, S. Jakobsen, K. P. Lillerud and C. Lamberti, Disclosing the complex structure of UiO-66 metal organic framework: a synergic combination of experiment and theory, *Chem. Mater.*, 2011, **23**, 1700–1718.

28 S. Mukherjee, S. Ghosh and S. Biswas, A MOF chemosensor for highly sensitive and ultrafast detection of folic acid in biofriendly medium, paper strips and real samples, *Inorg. Chem. Front.*, 2022, **9**, 6288–6298.

29 Z. Wu, D. Liang and X. Tang, Visualizing hydrogen sulfide in mitochondria and lysosome of living cells and in tumors of living mice with positively charged fluorescent chemosensors, *Anal. Chem.*, 2016, **88**, 9213–9218.

30 S. K. Mahato, D. Bhattacherjee and K. P. Bhabak, The biothiol-triggered organotrisulfide-based self-immolative fluorogenic donors of hydrogen sulfide enable lysosomal trafficking, *ChemComm*, 2020, **56**, 7769–7772.

31 J.-H. Cha, D.-H. Kim, S.-J. Choi, W.-T. Koo and I.-D. Kim, Sub-parts-per-million hydrogen sulfide colorimetric sensor: lead acetate anchored nanofibers toward halitosis diagnosis, *Anal. Chem.*, 2018, **90**, 8769–8775.

32 C. Tang, Y. Qin, C. Ni and J. Zou, Detection and removal of mercury ions in water by a covalent organic framework rich in sulfur and nitrogen, *ACS Appl. Polym. Mater.*, 2022, **4**, 849–858.

33 G. Marimuthu, M. Arivanandhan and C. Vedhi, Chemical vapor deposition of β-HgS nanoparticles from a precursor, bis (cinnamylpiperazinedithiocarbamato) mercury(II), *Synth. React. Inorg., Met.-Org., Nano-Met. Chem.*, 2015, **45**, 217–224.

34 L. Trnková, I. Boušová, V. Staňková and J. Dršata, Study on the interaction of catechins with human serum albumin using spectroscopic and electrophoretic techniques, *J. Mol. Struct.*, 2011, **985**, 243–250.

35 T. A. Wani, A. H. Bakheit, S. Zargar, M. A. Hamidaddin and I. A. Darwish, Spectrophotometric and molecular modelling studies on in vitro interaction of tyrosine kinase inhibitor linifanib with bovine serum albumin, *PLoS One*, 2017, **12**, e0176015.

36 M. Maity, S. Dolui and N. C. Maiti, Hydrogen bonding plays a significant role in the binding of coomassie brilliant blue-R to hemoglobin: FT-IR, fluorescence and molecular dynamics studies, *Phys. Chem. Chem. Phys.*, 2015, **17**, 31216–31227.

37 A. Rana, S. Ghosh and S. Biswas, An eco-friendly approach using a nonfluorous self-cleaning metal–organic framework composite and membrane for oil–water separation, *Inorg. Chem. Front.*, 2023, **10**(2), 612–620, DOI: **https://doi.org/10.1039/d2qi02062a**.

38 S. Mukherjee, K. Sarkar and S. Biswas, A fluorophore anchored MOF for fast and sensitive sensing of Cu(ii) and 3-nitrotyrosine in a physiological medium, *Dalton Trans.*, 2023, DOI: **DOI https://doi.org/10.1039/D3DT00660C**.